C. R. Physique 13 (2012) 237–245

Contents lists available at SciVerse ScienceDirect

Comptes Rendus Physique

www.sciencedirect.com

Use of large scale facilities for research in metallurgy

On the interest of synchrotron X-ray imaging for the study of solidification in metallic alloys

De l'intérêt de l'imagerie X synchrotron pour l'étude de la solidification d'alliages métalliques

Henri Nguyen-Thi [a,b,*], Luc Salvo [c], Ragnvald H. Mathiesen [d], Lars Arnberg [e], Bernard Billia [a,b], Michel Suery [c], Guillaume Reinhart [a,b]

[a] *Aix Marseille University, IM2NP, campus Saint-Jérôme, 13397 Marseille cedex 20, France*
[b] *CNRS, IM2NP, campus Saint-Jérôme, 13397 Marseille cedex 20, France*
[c] *Université de Grenoble – CNRS, laboratoire SIMAP-GPM2, 101, rue de la physique, 38402 Saint-Martin d'Hères cedex, France*
[d] *Department of Physics, NTNU, N-7491 Trondheim, Norway*
[e] *Department of Materials Technology, NTNU, N-7491 Trondheim, Norway*

ARTICLE INFO

Article history:
Available online 28 January 2012

Keywords:
Solidification
Synchrotron
Radiography
Topography
Tomography
Microstructure
Alloys

Mots-clés :
Solidification
Synchrotron
Radiographie
Topographie
Tomographie
Microstructure
Alliages

ABSTRACT

Recent developments of more powerful synchrotron sources have led to vast improvements in the performance of X-ray imaging. This is manifested by a continuous increase in the impact of synchrotron experiments in many research areas on materials, in particular solidification science. X-ray imaging has been established as a method of choice for in situ and real-time studies of solidification microstructure formation in metallic alloys, with spatio-temporal resolutions at the scales of relevance. In this article, we present illustrative results of the current capabilities of synchrotron X-ray imaging in this field of research, each of them using different X-ray techniques (radiography, topography and tomography). Those results demonstrate the high potential of these techniques for the investigation of dynamical phenomena in materials processing.

RÉSUMÉ

Les récents développements de sources synchrotron plus puissantes ont apporté une amélioration considérable des performances en imagerie X. Ceci s'est traduit par une augmentation continue de l'impact scientifique des expériences effectuées avec une source synchrotron dans de nombreux domaines de recherche sur les matériaux, et en particulier l'étude de la solidification. Il est bien établi que l'imagerie X est une méthode de choix pour les études in situ et en temps réel de la formation des microstructures de solidification dans les alliages métalliques, avec des résolutions spatio-temporelles pertinentes. Dans cet article, nous présentons des résultats illustrant les capacités actuelles de l'imagerie X synchrotron dans de ce domaine de recherche, chacun d'entre eux utilisant des techniques différentes (radiographie, topographie et tomographie X). Ces résultats démontrent le fort potentiel de ces techniques d'analyse pour l'investigation de phénomènes dynamiques en science des matériaux.

* Corresponding author at: Aix Marseille University, IM2NP, campus Saint-Jérôme, 13397 Marseille cedex 20, France.

1631-0705/$ – see front matter
doi:10.1016/j.crhy.2011.11.010

1. Introduction

Structural materials are primarily used because of their good mechanical behaviour resulting from their ability to sustain and/or transmit forces with negligible damage. It is well known that properties of the grown material are largely controlled by the microstructure(s) left in the solid during processing. Thus, a precise mastering of the solidification is essential to tailor products in a reproducible fashion to a specified quality. Beyond technological interest, the solidification patterns that dynamically form at the solid–liquid interface relate to non-linear physics and belong to the field of self-organisation in systems far from equilibrium [1,2]. One major difficulty in this study is the real-time and in situ observation of the interface, especially for metallic alloys. Classical analysis, such as quenching or decanting techniques, do not provide the interface evolution over time, but gives only a "frozen" picture of the solid microstructure.

The Peltier Interface Demarcation technique enables one to follow the time evolution of the solid–liquid interface, but requires a tedious and time-consuming post-mortem metallographic procedure [3]. Transparent organic materials [4] have been successfully used to study directional solidification but their behaviour is not completely identical to metallic systems in particular due to their low thermal conductivity. In addition, it is difficult with these alloys to analyse critical phenomena such as the influence of stress and strains on solidification microstructure dynamics [5]. It has now become evident that in situ and real-time X-ray imaging, with the increased capabilities of 3rd generation synchrotrons (high transversal coherence of the beam, high brilliance, etc.), should be retained as the method of choice to investigate the dynamics of the solidification front of metallic alloys grown from the melt. In the first part of the paper, the principles of radiography [6–8], white beam topography [9–11] and tomography [12], will be briefly described. Then, a selection of some recent results obtained at the European Synchrotron Radiation Facility (ESRF, Grenoble, France) will be given, illustrating the high capabilities of these X-ray imaging techniques in the field of metallic alloy solidification.

2. Principles of X-ray imaging techniques

2.1. Absorption and phase contrast radiography

Since their discovery, X-rays have been used to record radiographs displaying absorption contrasts. Conventional absorption radiography is a non-destructive technique based on local changes in the amplitude of the X-ray beam transmitted through the sample. A (monochromatic) X-ray beam illuminates the sample and a 2D-detector (photographic film, nuclear plate or CCD camera) is placed close to the sample. In alloy systems, contrast mainly results from segregation of the chemical species [13–16] and is generally weak and therefore difficult to reveal with conventional X-ray sources. The high intensity of synchrotron radiation makes it possible to record images with enough contrast in reasonable time (50–100 ms), which is crucial for studying dynamical phenomena. When such recordings are carried out at third generation synchrotron sources, phase contrast can also be obtained. This is due to the large transverse coherence of the synchrotron beam (typically $\approx$ 100–300 µm at ID19 beamline of ESRF), which allows (without additional devices) sample features to be visualised directly (phase object) by the X-ray phase modification thereby induced in the monochromatic transmitted beam [17,18]. Thus contrasts arise from interference between parts of the wave front which have experienced different phase shifts due to refraction. In this imaging technique, the experimental device is similar to the absorption radiography system with the exception of the distance between the sample and the detector, which must be adjusted owing to the characteristic spatial frequencies of the analysed sample.

2.2. White beam topography

X-ray white beam topography has long been known as a non-destructive imaging technique, which allows the long strain field around defects to be characterised as well as weak distortions present in bulky crystalline samples [19]. Therefore, this technique has been widely used to study the relationships between defects (dislocations, twins, stacking faults, inclusions or precipitates), crystal growth mechanisms and crystal properties.

Synchrotron X-ray topography technique is the method of choice giving access to solidification microstructure disorientations because any small change in cell or dendrite orientation with respect to the incident X-ray beam generates a displacement of its Laue images. The high flux available at synchrotron sources has made it possible to record in one shot with an exposure time of about one second several diffraction spots for a large volume of the sample (a few $\mathrm{cm}^2 \times 0.1$ cm), a large sensitivity range ($< 10^{-6}$–10^{-3}) and a spatial resolution in the micrometer range. Each diffraction spot may give different contrasts and thus complementary information about strains and misorientations in the solidification microstructure [11]. Moreover, the long source–sample distance (about 150 m at ID19, ESRF), added to the small dimensions of the source (less than 0.1 mm), provides highly coherent beam allowing to work at large sample–detector distances retaining a high geometrical resolution. This is particularly appropriate to the in situ study of directional solidification, since the sample is generally located inside a bulky UHV-furnace.

E-mail addresses: henri.nguyen-thi@im2np.fr (H. Nguyen-Thi), luc.salvo@simap.grenoble-inp.fr (L. Salvo), ragmat@phys.ntnu.no (R.H. Mathiesen), Lars.arnberg@material.ntnu.no (L. Arnberg), Bernard.billia@im2np.fr (B. Billia), Michel.suery@grenoble-inp.fr (M. Suery), guillaume.reinhart@im2np.fr (G. Reinhart).

Recently, a unique experimental setup, which allows the combination of synchrotron X-ray radiography and topography, has been implemented at the ID19 imaging beamline of the ESRF [20]. The example given in this paper relies on the complementary information simultaneously provided by the association of these two synchrotron X-ray imaging techniques.

2.3. Tomography

The principle of X-ray tomography is to take several hundred radiographs (named a scan) while rotating the sample over 180° or 360° and use them to retrieve a 3D image of the material using specific algorithm. The main advantage of X-ray tomography in comparison with other techniques that allow getting 3D images such as serial sectioning [21–25] is that it is non-destructive and it allows performing in situ experiments. Details about X-ray tomography can be found in [26]. In this article we will focus on solidification studies for which there are mainly two ways to use tomography: post-mortem observations and in situ continuous observation. In post-mortem tomography, a conventional scan lasting of the order of 30 minutes for a 1 μm spatial resolution is made at room temperature on solidified samples. This can be performed with a synchrotron or a laboratory source and allows investigating final microstructures [27–30]. However, it is very difficult to study what happens during solidification by quenching the specimen since this requires very fast cooling rates (over 100 °C/s [31]) to freeze the microstructure. Such high cooling rates are very difficult to obtain except in very small specimens. The only way to perform in situ studies of solidification phenomena with tomography is to reduce the time to acquire a complete scan in less than 30 seconds for cooling rates of the order of a few degrees/min. In this condition, microstructural changes during the acquisition of one scan are small enough to obtain a non-blurred reconstructed image. In 2002 these conditions were obtained thanks to specific CCD cameras which allow reducing drastically acquisition time of a scan down to approximately 20 seconds. By using a specific furnace mounted on the tomograph, it was possible to image for the first time in 3D the microstructure of an Al–Cu alloy during solidification [32] with a spatial resolution of the order of 3 μm. Nowadays scans can be performed with a spatial resolution of about 1 μm with nearly the same acquisition time. These conditions allow observations and quantification of local microstructural changes occurring during solidification of Al alloys [33,34]. However, despite this fast acquisition limitations still exist in terms of cooling rate as already mentioned and for the study of the early stages of solidification during which dendrites are moving too much during a scan.

3. Selection of recent results obtained with the various synchrotron X-ray imaging techniques

3.1. Columnar dendritic growth under impact of buoyant flow

Alloys may show appreciable differences between the density of the primary phase and that of the bulk- or solute enriched melt. During primary phase growth, excess solute beyond the primary phase solubility is rejected at the growth front and transported back into the melt by diffusion. A boundary layer of enriched solute builds up ahead of the progressing solid–liquid interface, and in turn the shape of this boundary layer is interrelated to the solid–liquid interface progression and morphology. Depending on the enriched melt density with respect to the nominal melt composition and the growth direction relative to gravity, enriched solute may either settle further into the mushy zone or eject out of the mush and into the bulk liquid. In the latter case, the buoyant liquid flow will interact with diffusive mass transport from the columnar front, and therefore impact on the local columnar dendrite tip velocities, dendrite morphologies and primary arm spacing. The situation is rather complex since flow in and out of the mush also addresses the mushy-zone flow permeability, i.e. the impact on the flow asserted by the geometry of the dendrite network.

The effects of such flows were investigated in synchrotron video microscopy study of directional solidification parallel to gravity in a near-eutectic Al–30 wt% Cu alloy at the ID22 beamline at ESRF [16] (Fig. 1). The figure shows a selection of radiographs from the full video sequence, revealing a progressing columnar dendritic interface with three parallel primary trunks, trailed by a near-planar eutectic front and ahead of and in between the dendrites one can observe the flow and diffusion driven changes of the Cu-concentration in the melt.

It should be noted that while the dendritic front and the Cu constitutional field mainly appear due to absorption contrast, the eutectic front, apparent in the radiographs of Fig. 1 as bright lines closely horizontally oriented, are made visible mainly by phase contrast arising from average density differences between solid and liquid regions with roughly the same eutectic composition [16]. The setup and experimental configuration employed for these experiments gave a nominal spatial resolution of $\Delta r_n \sim 1.4$ μm and a temporal resolution of 0.45 s, including a 0.15 s detector read-out dead time between consecutive frames. However, with $t_{\text{exp}} = 0.3$ s frame exposures and dendritic tip and eutectic interface velocities in the range $v_{int} \sim 2.5$–100 μm/s, temporal blurring, $\Delta r_t = v_{int} t_{\text{exp}}$ tended to dominate the obtainable spatial resolution [16].

The contrasts obtained in this study allowed for extraction of several quantitative data by image processing. The initial step involved a binary image segmentation of the 2D radiograms distinguishing pixels representing a fully molten projection volume from those that contained a combination of solid and liquid or was fully solid. Following the binarisation, solid–liquid coordinates could be extracted directly by a gradient operation on the binary masks. The full time evolution of the 2D projected solid–liquid interface is shown in Fig. 1(c). From the coordinates, dendrite tip curvatures could be determined by a least squares fitting of parabolas to the tip coordinates, while the eutectic front was traced by a first order polynomial.

Dendritic tip and eutectic front velocities could be extracted from a frame-by-frame tracing of the parabola loci and the eutectic front polynomial. The binary mask could also be employed to extract a 3D *yzt* volume of the liquid similar to the

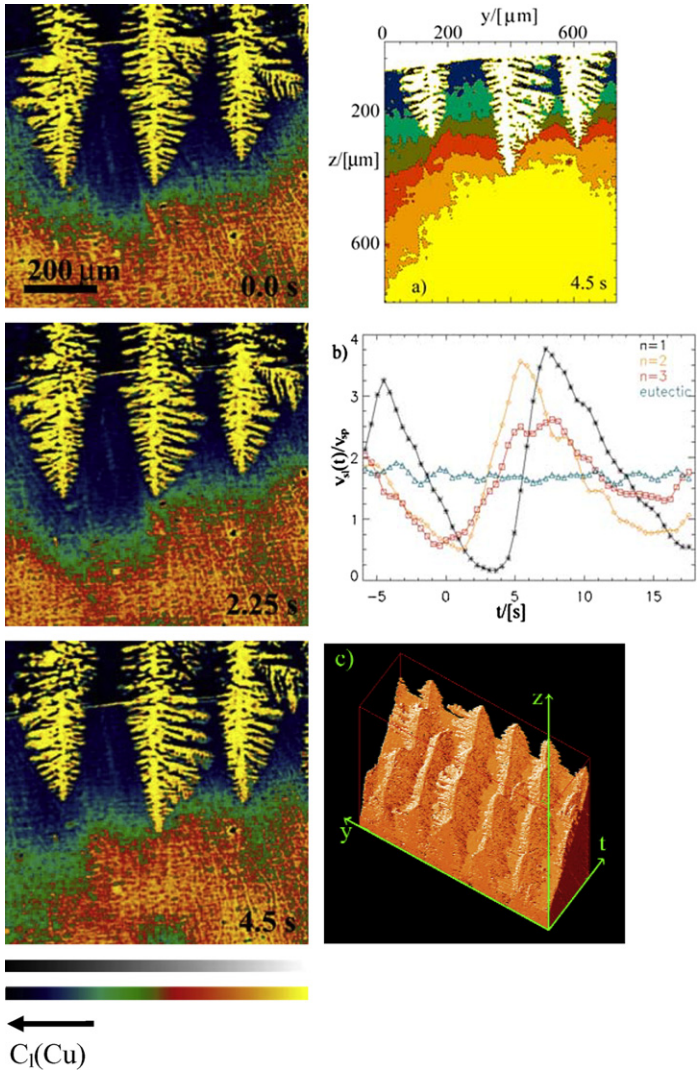

Fig. 1. Left column: X-ray radiographs showing planar eutectic and columnar dendritic growth during directional solidification parallel to gravity in Al–30 wt% Cu showing microstructure evolution at times $t_0, t_0 + 2.25$ s, $t_0 + 4.5$ s. The images also display the local liquid concentration, C_l(Cu), in a relative manner (colour contrast relates to greyscale as indicated by horizontal bars at the bottom left). Right column: Examples of quantitative information extracted by image processing: (a) 2D projected melt compositional contour map at $t_0 + 4.5$ s, starting at $C_l \leqslant 33$ wt% Cu (black) and with increments of -0.5 wt% Cu; (b) Velocities for the eutectic front and columnar tips 1–3, enumerated from left to right and normalised by the sample pulling velocity, $V_{sp} \sim 22.5$ µm/s; (c) Time-evolution of the 2D solid–liquid interface projections where the y and z dimensions of the box correspond to the field of view of 1.5×1.35 µm^2, whereas the box size along the time axis, t, corresponds to the full length of the video sequence, 54 s [16].

Fig. 1. Colonne de gauche : Radiographies X montrant la croissance d'un front eutectique plan et de dendrites colonnaires au cours d'une solidification dirigée parallèle à la gravité dans un alliage Al–30 %pds Cu montrant l'évolution de la microstructure aux temps t_0, $t_0 + 2.25$ s et $t_0 + 4.5$ s. Les images présentent aussi la concentration locale du liquide, C_l(Cu), de manière relative (le contraste en couleurs est lié au niveau de gris comme indiqué par la barre horizontale en bas à gauche). Colonne de droite : exemples d'information quantitatives extraites par traitement d'image : (a) projection 2D de la carte de contour en composition du liquide à $t_0 + 4.5$ s, commençant à $C_l \leqslant 33$%pds Cu (noir) avec des incréments de -0.5 %pds Cu ; (b) Vitesses des front eutectique et des pointes colonnaires 1–3, numérotées de gauche à droite et normalisées par la vitesse de tirage de l'échantillon, $V_{sp} \sim 22.5$ µm/s ; (c) Evolution temporelle des projections de l'interface solide-liquide 2D.

3D *yzt* solid rendering volume shown in Fig. 1(c). After a normalisation towards the X-ray transmission through bulk liquid, the 3D *yzt* liquid volume could be transferred from normalised X-ray transmission intensities into Cu concentration data by a simple logarithmic relationship to the normalised intensities, deduced from conventional X-ray absorption.

All together data extracted from the quantitative image analysis was used to demonstrate the relations between local settling Cu-enriched melt flow out of the mushy zone and the growth characteristics of the columnar dendritic array. The trends observed in the study have been confirmed and further elaborated by phase field simulations [35]. Furthermore, in experiments with columnar growth directed opposite to gravity, dendrite fragmentation was found to be a prominent mechanism used to accommodate incoming solute flow [36–38].

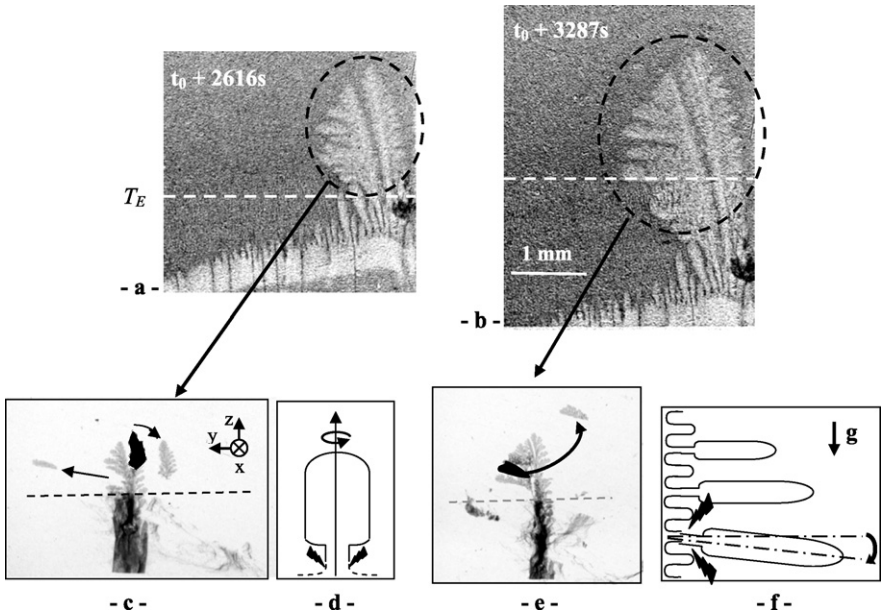

Fig. 2. Radiographs (Figs. 2a and 2b) and topographs (Fig. 2c and Fig. 2e) of a dendritic microstructure during solidification (Al–3.5 wt% Ni, temperature gradient is about 30 K/cm, and pulling rate is 1 μm/s) showing the bending and the rotation of a secondary arm of the left dendrite, as well as the rotation of a portion of the primary trunk of the right dendrite.

Fig. 2. Radiographies (Figs. 2a et 2b) et topographies (Fig. 2c et Fig. 2e) d'une microstructure dendritique au cours de la solidification (Al–3,5 %pds Ni, pour un gradient de température de 30 K/cm et une vitesse de tirage de 1 μm/s) montrant la flexion et la rotation d'un bras secondaire de la dendrite de gauche ainsi que la rotation d'une portion de la dendrite de droite.

3.2. Stresses and strains induced by microstructure formation

Strains and stresses are common phenomena in solidified materials. Plenty of factors can be at their origin such as solid state phase transformations or natural cooling down to room temperature. It follows that those accompanying the formation of the growth microstructure are blurred after complete processing, and then delicate to identify and characterise. Critical information on the mechanical effects and crystalline defects that make a solidifying system strikingly different from a fluid–fluid system can be unveiled by combining synchrotron X-ray radiography and topography [10,11]. While evolution of the solid–liquid interface morphology is continuously monitored by radiography, a series of topography snapshots at selected instants provide parallel information on the formation and evolution of mechanical features. As an example, Fig. 2 shows radiographs and topographs of the solidification microstructure at two different instants during the growth of an Al–3.5 wt% Ni sample, in a temperature gradient of 30 K/cm and a pulling rate of about 1 μm/s. In the radiographs (Figs. 2a and 2b), one can see that the solidification microstructure is not uniform across the transverse direction (clustering phenomenon) due to convection effect [39]. It consists of two dendrites located at the right-hand side of the image, protruding markedly into the liquid phase (steepling phenomenon) and with a eutectic front at the base of the solidification front (indicated by a dashed line). In the topographs (Figs. 2c and 2e), one can see that the Laue images of a secondary arm of the left dendrite and a portion of the primary trunk of the right dendrite are shifted from the main dendrite image, whereas the structure remains fully connected in radiography. This observation means that the crystallographic orientations of those two parts have changed during the growth. By analysing the displacement of Laue images on different diffraction spots, we have been able to establish that the portion of primary trunk has achieved a rotation of some tenth of degrees around its growth axis (Fig. 2d). This rotation is reversible since the Laue image of the portion of the primary trunk reappears at its initial location on the topograph Fig. 2e. It can be interpreted as an elastic mechanism resulting from the action of the torque induced by shear stress that builds up with the growth shape, as previously suggested by Billia et al. [40]. Another disorientation mechanism is highlighted by the analysis of the displacement of the secondary arm in the topographs (Figs. 2c and 2e). We have been able to establish that the entire arm has rotated by 3 degrees around the incident direct beam axis Ox and 0.3 degree around the y-axis perpendicular to the direct incident-beam. The rotation around the incident beam axis is also visible on radiographs, which are actually projections of the structure along the incident beam. This phenomenon occurs rapidly (less than 1 second), and the successive rotation of secondary arms is usually observed during the growth of dendritic microstructures (Fig. 3). The origin of this disorientation is the bending mechanism described by Billia et al. [40]. In our case, horizontal secondary arms generate an extrinsic mechanical bending moment caused by gravity. Because of the lower moment of inertia there, stresses are localised at the thin solid necks that attach the arms to the primary trunk, and cumulate as the arms grow and become heavier. After a certain time, the yield stress is exceeded at the necks, which causes their sudden and irreversible rotation, carrying the entire single crystal along with it (Figs. 2(e) and 3). An estimation of the

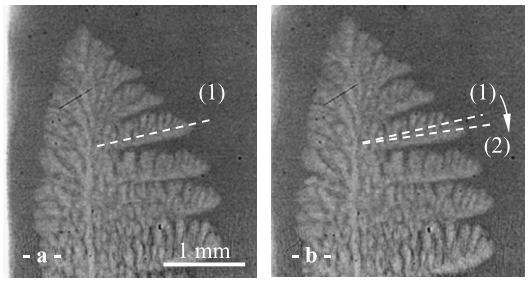

Fig. 3. Radiographs showing the bending of a secondary arm of a dendrite during solidification (Al–3.5 wt% Ni, in a temperature gradient of about 27 K/cm and a pulling rate of 1,7 μm/s). The time elapsed between the two pictures is about 21 seconds.

Fig. 3. Radiographies montrant le fléchissement d'un bras secondaire d'une dendrite de 5,5° au cours de sa croissance (Al–3,5 %pds Ni, pour un gradient de température de 27 K/cm et une vitesse de tirage de 1,7 μm/s). Le temps écoulé entre les deux images est de 21 secondes.

bending stress σ_B at the neck can be analytically performed by considering secondary arms as parallelepipeds connected to the primary trunk by a thin cylindrical neck [11]. The bending stress is found to be in the range: 0.02 MPa $< \sigma_B <$ 0.27 MPa. The large difference between the estimated minimum and maximum values is due to the inaccuracy in the measurement of the neck radius r and the variation in r^4 of the moment of inertia, which has a strong effect on the value of σ_B. Nevertheless, this estimation gives us an order of magnitude for the elastic limit of aluminum near the melting point. The maximum value is of the same order of magnitude as the yield stress at the melting point (0.6 MPa) used by Pilling and Hellawell [41] by reducing by an order of magnitude the value extrapolated from low temperature data, or the value of 0.13 MPa obtained by Billia et al. [40] for the bending of cells during horizontal solidification of Al–Cu alloys. Our estimation shows that the low stress caused by gravity is sufficient to provoke disorientations of several degrees of parts of dendritic microstructures, and can, therefore, induce the growth of adjacent dendrites with different crystallographic orientation. This will eventually lead to misalignments between dendrites comparable with those observed after growth on real super-alloy blades [42,43]. Numerical methods can be used to model stresses and strains during growth as recently performed by Yang et al. [44] who used a finite element model to calculate stress and strain fields in moderate agitated fluid. The development of a numerical code to estimate strains and stresses during the development of structures with a complex dendritic morphology has yet to be done.

3.3. Examples for tomography

In situ solidification experiments were carried out on two types of samples with the aim to investigate two different phenomena. The first sample is a binary Al–8 wt% Cu alloy solidified in conventional condition thus leading to the nucleation, growth and coalescence of the dendrites until the final formation of the eutectic mixture. The second sample is a complex Al–8Si–4Cu–0.8Fe (wt%) designed to study the nucleation and growth of the Fe-rich intermetallic phase [34]. In both cases, a small cylindrical specimen ($\sim$ 3 mm long, $\sim$ 1.5 mm diameter) was machined from the initial casting and glued on top of an alumina rod. The experimental set-up is similar to that used in previous work [33]. In the synchrotron X-ray beam line, the sample was gradually heated until it becomes fully liquid. It is then held for a few minutes to ensure complete melting had occurred. The sample remains close to its original shape throughout the experiment due to the self-supporting nature of its oxide skin. The sample was then cooled at a controlled rate of about 1.5 °C/min for Al–8Si–4Cu–0.8Fe and 1 °C/min for Al–8 wt% Cu and microtomography image data were continuously gathered during the complete cooling process. Slow cooling was applied to ensure that the microstructural evolution between each time step (of the order of 1 min) was kept to a minimum. Experiments were performed on ID19 at ESRF with an optics of 1.4 μm. 600 projections were taken for one scan and a field of view of 1024 $\times$ 1024 pixel was set with FreLoN camera in the Fast Transfer Mode.

3.3.1. Al–Cu alloy

Fig. 4 shows the results of the experiment in the form of: (a) to (d) longitudinal 2D sections of the sample at various temperatures, (e) to (g) 3D images of the liquid corresponding to three temperatures in the solidification range. Owing to the time required for a scan to be recorded, good images for further image analysis can not be obtained for solid fractions lower than about 50%: indeed below this solid fraction solid particles grow too fast or move during the acquisition of a scan. The first image in Fig. 4(a) obtained at 608 °C corresponds to a solid fraction of about 65%. At this temperature, the dendrites are very well defined but the contrast between the solid and the liquid is quite weak since the difference in Cu content between the two phases is not very large. With decreasing temperature, the solid fraction increases and the contrast between the two phases increases. Finally at 548 °C, the eutectic mixture forms in between the primary already coalesced dendrites. The resolution allows showing clearly that the eutectic is constituted of two different phases but it is not high enough to distinguish them precisely. The 3D images of the liquid phase (Figs. 4(e)–(g)) show its evolution during solidification. One interesting aspect is the gradual formation of liquid arms with dead ends which will not play a role in the permeability of the solid skeleton. This effect was already mentioned when comparing permeability calculations based on real liquid distribution in a specimen with general equations such as that proposed by Carman and Kozeny [26].

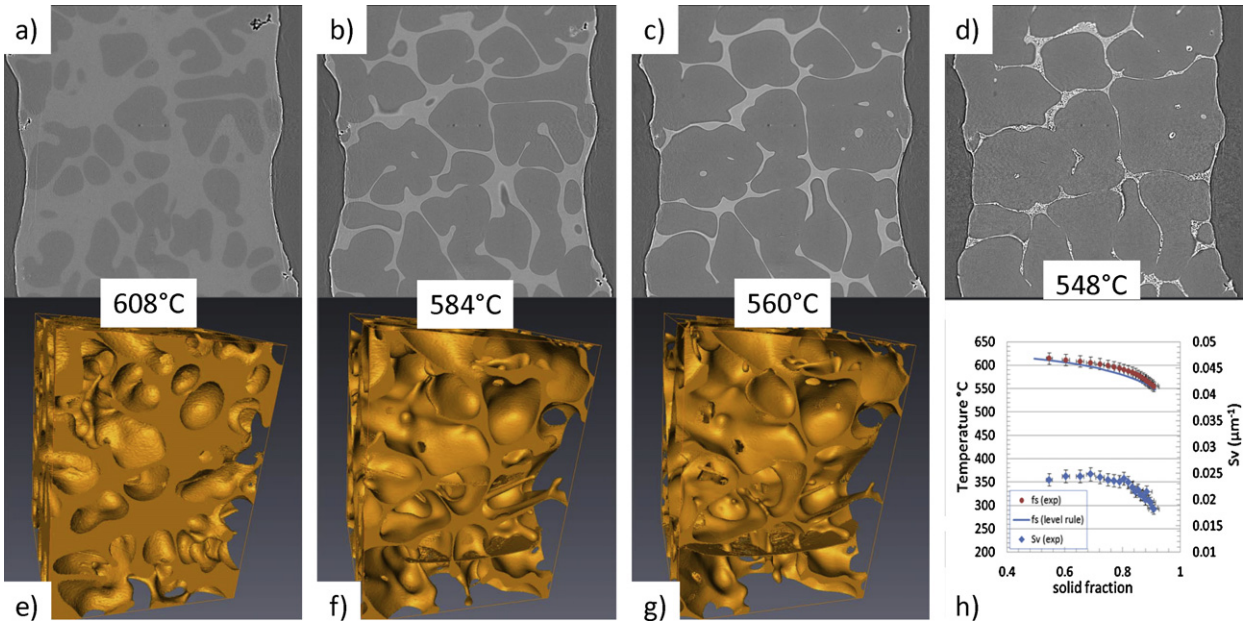

Fig. 4. In situ solidification of an Al–8 wt% Cu alloy: (a)–(d) 2D cross section at various temperatures (width of the image 1.4 mm), (e)–(g) 3D rendering of the liquid phase at the same temperatures than (a)–(c) (width of the box 1 mm), (h) temperature and solid–liquid interface area versus solid fraction. Lever rule estimation of solid fraction versus temperature is also shown in (h).

Fig. 4. Solidification *in situ* d'un alliage Al–8 %pds Cu : (a)–(d) Section 2D à différentes températures (largeur de l'image 1,4 mm), (e)–(g) reconstruction 3D de la phase liquide pour les mêmes températures que (a)–(c) (largeur de la boîte 1 mm), (h) température et surface de l'interface solide liquide en fonction de la fraction solide. L'estimation par la règle des leviers de la fraction de solide avec la température est aussi montrée sur cette figure.

Fig. 4(h) presents the 3D quantitative analysis obtained from these in situ experiments. A 3D median filter was applied on the volume in order to reduce noise in the images, and then the liquid and primary solid phases were distinguished by applying a conventional threshold on the grey level. The AVIZO software was used for the 3D rendering and to quantify the solid fraction and the solid–liquid interface area. Experimental temperature — solid fraction curve is very close to the classical lever rule which is expected since the cooling rate is very slow (1.4 °C/s). The variation of the solid–liquid interface area as a function of the solid fraction is more interesting. The curve is not symmetric with respect to the 0.5 solid fraction which indicates that the rate of growth of the solid at low solid fraction is not equal to the rate of disappearance of the liquid at large solid fraction. This result was already reported and attributed to the fact that the shape of the two phases (liquid and solid) is not similar [33].

3.3.2. Al–Si–Cu–Fe alloy

Fig. 5 shows a sequence of images obtained during solidification: (a) to (d) are 2D sections at various temperatures whereas (e) to (h) correspond to 3D images of Al_5FeSi platelets at the same temperatures or solidification times (time $t = 0$ is taken when the primary solid phase appears, in this case at 594 °C). During solidification, the first reaction that is observed in the images is the growth of the primary aluminium dendrites which appear slightly darker than the liquid (Fig. 5(a)). The second observed reaction is the nucleation and growth of several Al_5FeSi platelets, which appear very bright and in high contrast against the darker background of the aluminium dendrites and liquid (Fig. 5(b)). When temperature decreases, the number of plates increases and they grow (Figs. 5(b)–5(d)) while growth and coarsening of the dendrites continue. The contrast between the dendrites and the remaining liquid increases, owing to the progressive enrichment in Cu of the liquid. These observations allow investigating in details the nucleation and growth of complex intermetallic phases therefore getting a better understanding of the involved mechanisms. Furthermore 3D image analysis has been performed to quantify nucleation and growth of the intermetallic plates. After a 3D median filter applied to the volume in order to reduce noise in the images, a conventional threshold has been applied on the grey level which is enough to distinguish the intermetallics from the liquid, the primary solid phase and even the Al–Si eutectic. Then in-house routines developed in ImageJ software have been used to quantify the number of platelets and their volume fraction. 3D rendering has been obtained on these images using AVIZO software. Fig. 5(i) presents thus the variation of the number of intermetallic plates per mm^3 and their volume fraction as a function of time (time $t = 0$ is taken when the first primary solid appears at 594 °C). As it can be seen there is a time required for nucleation (about 5 min) and then continuous nucleation of platelets occurs during solidification. The nucleation site is the oxide skin of the sample for all the platelets and the experimental temperature for nucleation (583.9 °C) is in accordance with Thermocalc simulation for this system (583.1 °C) [34]. The volume fraction of platelets increases smoothly with time as shown in Fig. 5(i) but it has been shown that in fact the growth rate of an intermetallic plate is not constant due to interaction with the primary phase [34].

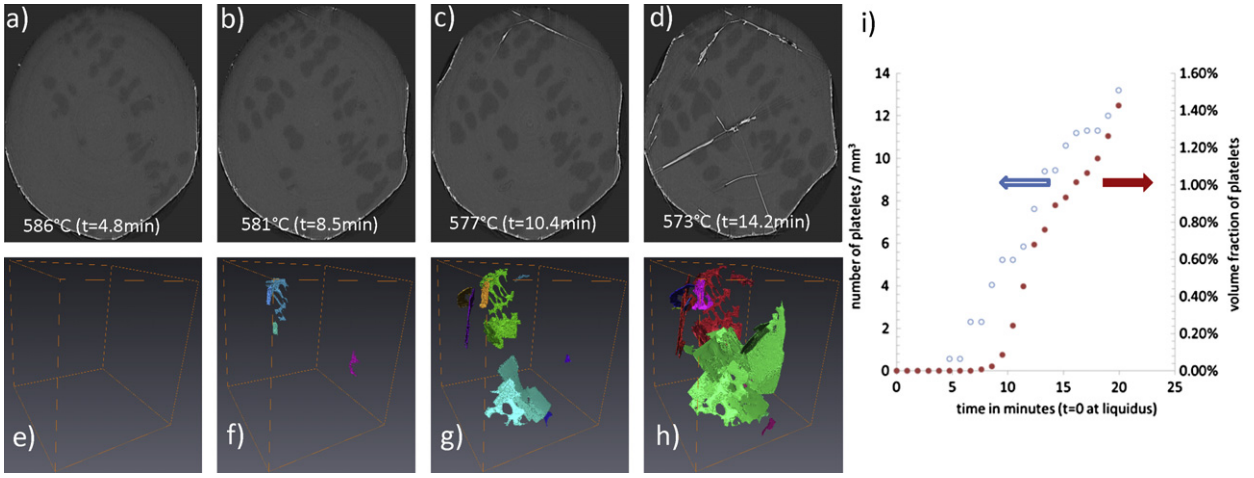

Fig. 5. In situ solidification of an Al–8Si–4Cu–0.8Fe (wt%) alloy: (a)–(d) 2D cross section at various temperatures (width of the image 1.4 mm), (e)–(h) 3D rendering of intermetallic plates at the same temperatures than (a)–(d) (width of the box ~ 1 mm). (i) Number of intermetallics plates per mm^3 (hollow circle) and volume fraction (plain circle) with time (time $t = 0$ is taken when the first primary phase appears at $T = 594\,^{\circ}$C).

Fig. 5. Solidification in situ d'un alliage Al–8Si–4Cu–0.8Fe (%pds) : (a)–(d) section 2D à différentes températures (largeur de l'image 1,4 mm), (e)–(h) reconstruction 3D de plaquettes intermétalliques aux mêmes températures que (a)–(d) (largeur de la boîte 1 mm). (i) nombre de plaquettes intermétalliques par mm^3 (cercles vides) et fraction volumique (cercle pleins) en fonction du temps ($t = 0$ correspond à l'apparition de la première phase primaire à $T = 594\,^{\circ}$C).

4. Conclusion

X-ray imaging techniques, as recently enhanced by the advent of third-generation synchrotron sources, have proved to be powerful techniques for the characterisation of dynamical phenomena during metallic alloy solidification. The various techniques presented in this paper (radiography, topography and tomography) give complementary information on the microstructure formation and evolution at various length and time scales. A key and challenging issue in these techniques is the quantitative extraction of data from 2D or 3D images, such as segregation, stresses and strains, etc. Much effort has to be carried on in this direction to obtain benchmark data, which can be used for guidance and validation of numerical codes.

Acknowledgements

The authors gratefully acknowledge all their colleagues at IM2NP, NTNU and Grenoble INP who participated to the synchrotron experimental campaigns, without them this paper could not have been written. Part of this work was partially funded by the European Space Agency (XRMON contract).

The authors wish to thank ESRF Grenoble for providing beam time within the Long Term Project MA560 and all staff members of the ID19 beamline for their technical support. Part of this work was also carried out in the framework of the projects ANR-05-BLAN-0286-01 “TOMOSOLIDAL” and ANR-08-BLAN08-2_318938 “SIMUZAL” supported by the Agence Nationale de la Recherche, which is gratefully acknowledged. They also would like to thank S. Terzi and F.X. Hoche who participate to the 3D data analysis.

References

[1] W.W. Mullins, R.F. Sekerka, Stability of a planar interface during solidification of a dilute binary alloy, J. Appl. Phys. 35 (1964) 444.
[2] J.S. Langer, Lectures in the theory of pattern formation, in: J.V.a.R.S.J. Souletie (Ed.), Chance and Matter, Les Houches Summer School, North Holland, Amsterdam, 1986, p. 629.
[3] Y. Dabo, H. Nguyen Thi, S.R. Coriell, G.B. McFadden, Q. Li, B. Billia, Microsegregation in Peltier interface demarcation, Journal of Crystal Growth 216 (2000) 483–494.
[4] K.A. Jackson, J.D. Hunt, Transparent compounds that freeze like metals, Acta Metall. 13 (1965) 1212.
[5] L.M. Fabietti, R. Trivedi, In situ observations of stress-induced defect formation at the solid–liquid interface, Journal of Crystal Growth 173 (1997) 503–512.
[6] R.H. Mathiesen, L. Arnberg, K. Ramsokar, T. Weitkamp, C. Rau, A. Snigirev, Time-resolved X-ray imaging of dendritic growth in binary alloys, Phys. Rev. Lett. 83 (1999) 5062–5065.
[7] H. Yasuda, I. Ohnaka, K. Kawasaki, A. Sugiyama, T. Ohmichi, J. Iwane, K. Umetani, Direct observation of stray crystal formation in unidirectional solidification of Sn–Bi alloy by X-ray imaging, Journal of Crystal Growth 262 (2004) 645–652.
[8] T. Schenk, H. Nguyen Thi, J. Gastaldi, G. Reinhart, V. Cristiglio, N. Mangelinck-Noël, H. Klein, J. Härtwig, B. Grushko, B. Billia, J. Baruchel, Application of synchrotron X-ray imaging to the study of directional solidification of aluminium-based alloys, Journal of Crystal Growth 275 (2005) 201–208.
[9] G. Grange, J. Gastaldi, C. Jourdan, B. Billia, Evolution of characteristic pattern parameters in directional solidification of thin samples of a dilute Al–Cu alloy, Journal of Crystal Growth 151 (1995) 192–199.
[10] G. Grange, C. Jourdan, J. Gastaldi, B. Billia, Strain visualization of the onset of morphological instability and defect formation in cellular solidification of a dilute Al–Cu alloy, Acta Materialia 45 (1997) 2329.

[11] G. Reinhart, A. Buffet, H. Nguyen-Thi, B. Billia, H. Jung, N. Mangelinck-Noel, N. Bergeon, T. Schenk, J. Hartwig, J. Baruchel, In-situ and real-time analysis of the formation of strains and microstructure defects during solidification of Al–3.5 wt pct Ni alloys, Metallurgical and Materials Transactions A – Physical Metallurgy and Materials Science 39A (2008) 865–874.
[12] E. Maire, J.Y. Buffiere, L. Salvo, J.J. Blandin, W. Ludwig, J.M. Letang, On the application of X-ray microtomography in the field of materials science, Advanced Engineering Materials 3 (2001) 539–546.
[13] M.P. Stephenson, J. Beech, In situ radiographic observations of solute redistribution during solidification, in: J. Solidification Cast. Met. Conference Proceedings, Sheffields, UK, 1977, pp. 34–38.
[14] W.F. Kaukler, F. Rosenberger, X-ray microscopic observations of metal solidification dynamics, Metallurgical and Materials Transactions A – Physical Metallurgy and Materials Science 25 (1994) 1775–1777.
[15] S. Boden, S. Eckert, B. Willers, G. Gerbeth, X-ray radioscopic visualization of the solutal convection during solidification of a Ga–30 wt pct in alloy, Metallurgical and Materials Transactions A – Physical Metallurgy and Materials Science A 39 (2008) 613–623.
[16] R.H. Mathiesen, L. Arnberg, X-ray radiography observations of columnar dendritic growth and constitutional undercooling in an Al–30wt%Cu alloy, Acta Materialia 53 (2005) 947–956.
[17] P. Cloetens, R. Barrett, J. Baruchel, J.P. Guigay, M. Schlenker, Phase objects in synchrotron radiation hard X-ray imaging, J. Phys. D-Appl. Phys. 29 (1996) 133–146.
[18] A. Snigirev, I. Snigireva, V. Kohn, S. Kuznetsov, I. Schelokov, On the possibilities of X-ray phase contrast microimaging by coherent high-energy synchrotron radiation, Review of Scientific Instruments 66 (1995) 5486–5492.
[19] D.K. Bowen, B.K. Tanner, High Resolution X-Ray Diffraction and Topography, 1998.
[20] A. Buffet, G. Reinhart, T. Schenk, H. Nguyen Thi, J. Gastaldi, N. Mangelinck-Noël, H. Jung, J. Härtwig, J. Baruchel, B. Billia, Real-time and in situ solidification of Al-based alloys investigated by synchrotron radiation: A unique experimental set-up combining radiography and topography techniques, Phys. Stat. Sol. 204 (2008) 2721–2728.
[21] Y. Ito, M.C. Flemings, in: J.A. Sekhar, J. Dantzig (Eds.), Nature and Properties of Semi-Solid Materials, TMS, Warrendale, PA, 1991, p. 3.
[22] B. Niroumand, K. Xia, 3D study of the structure of primary crystals in a rheocast Al–Cu alloy, Mater. Sci. Eng. A-Struct. Mater. Prop. Microstruct. Process. 283 (2000) 70–75.
[23] J. Alkemper, P.W. Voorhees, Three-dimensional characterisation of dendritic microstructures, Acta Materialia 49 (2001) 897–902.
[24] A.V. Nagasekhar, C.H. Caceres, C. Kong, 3D characterisation of intermetallics in a high pressure die cast Mg alloy using focused ion beam tomography, Mater. Charact. 61 (2010) 1035–1042.
[25] J. Kastner, B. Harrer, H.P. Degischer, High resolution cone beam X-ray computed tomography of 3D-microstructures of cast Al-alloys, Mater. Charact. 62 (2011) 99–107.
[26] L. Salvo, M. Suery, A. Marmottant, N. Limodin, D. Bernard, 3D imaging in material science: Application of X-ray tomography, C. R. Phys. 11 (2010) 641–649.
[27] A. Chaijaruwanich, P.D. Lee, R.J. Dashwood, Y.M. Youssef, H. Nagaumi, Evolution of pore morphology and distribution during the homogenization of direct chill cast Al–Mg alloys, Acta Materialia 55 (2007) 285–293.
[28] G. Nicoletto, G. Anzelottia, R. Kone, X-ray computed tomography vs. metallography for pore sizing and fatigue of cast Al-alloys, Procedia Engineering (2010) 547.
[29] D. Fuloria, P.D. Lee, An X-ray microtomographic and finite element modeling approach for the prediction of semi-solid deformation behaviour in Al–Cu alloys, Acta Materialia 57 (2009) 5554–5562.
[30] D. Bernard, O. Nielsen, L. Salvo, P. Cloetens, Permeability assessment by 3D interdendritic flow simulations on microtomography mappings of Al–Cu alloys, Mater. Sci. Eng. A – Struct. Mater. Prop. Microstruct. Process. 392 (2005) 112–120.
[31] O. Pompe, M. Rettenmayr, Microstructural changes during quenching, Journal of Crystal Growth 192 (1998) 300–306.
[32] O. Ludwig, M. Dimichiel, L. Salvo, M. Suery, P. Falus, In-situ three-dimensional microstructural investigation of solidification of an Al–Cu alloy by ultrafast X-ray microtomography, Metallurgical and Materials Transactions A – Physical Metallurgy and Materials Science 36A (2005) 1515–1523.
[33] N. Limodin, L. Salvo, E. Boller, M. Suéry, M. Felberbaum, S. Gailliègue, K. Madi, In situ and real-time 3-D microtomography investigation of dendritic solidification in an Al–10 wt% Cu alloy, Acta Materialia 57 (2009) 2300–2310.
[34] S. Terzi, J.A. Taylor, Y.H. Cho, L. Salvo, M. Suery, E. Boller, A.K. Dahle, In situ study of nucleation and growth of the irregular alpha-Al/beta-Al5FeSi eutectic by 3-D synchrotron X-ray microtomography, Acta Materialia 58 (2010) 5370–5380.
[35] I. Steinbach, Pattern formation in constrained dendritic growth with solutal buoyancy, Acta Materialia 57 (2009) 2640–2645.
[36] R.H. Mathiesen, L. Arnberg, P. Bleuet, A. Somogyi, Crystal fragmentation and columnar-to-equiaxed transitions in AlCu studied by synchrotron X-ray video microscopy, Metall. Mater. Trans. A 37A (2006) 2515–2524.
[37] D. Ruvalcaba, R.H. Mathiesen, D.G. Eskin, L. Arnberg, L. Katgerman, Fragmentation due to the interaction of solute flow with the dendritic network during the solidification of aluminum alloys, in: H. Jones (Ed.), 5th Decennial Conference on Solidification Processing, University of Sheffield, Sheffield, UK, 2007, pp. 321–325.
[38] L. Arnberg, R.H. Mathiesen, The real-time, high-resolution X-ray, video microscopy of solidification in aluminum alloys, JOM 59 (2007) 20–26.
[39] H. Nguyen Thi, Y. Dabo, B. Drevet, M.D. Dupouy, D. Camel, B. Billia, J.D. Hunt, A. Chilton, Directional solidification of Al–1.5 wt% Ni alloys under diffusion transport in space and fluid flow localisation on Earth, Journal of Crystal Growth 281 (2005) 654–668.
[40] B. Billia, N. Bergeon, H. Nguyen Thi, H. Jamgotchian, Cumulative moments and microstructure deformation induced by growth shape in columnar solidification, Phys. Rev. Lett. 93 (2004) 126105.
[41] J. Pilling, A. Hellawell, Mechanical deformation of dendrites by fluid flow, Metallurgical and Materials Transactions A – Physical Metallurgy and Materials Science 27 (1996) 229–232.
[42] E. Blank, W. Kurz, M. Rappaz, Dendritic single-crystals-microstructure and deformation behavior, Helv. Phys. Acta 58 (1985) 469–483.
[43] N. Siredey, M. Boufoussi, S. Denis, J. Lacaze, Dendritic growth and crystalline quality of nickel-base single grains, Journal of Crystal Growth 130 (1993) 132–146.
[44] Z. Yang, C.G. Kang, Z.Q. Hu, Microstructural stress concentration: An important role in grain refinement of rheocasting structure, Metallurgical and Materials Transactions A 36 (2005) 2785–2792.